

Adaptive bandwidth management for entanglement distribution in quantum networks

Navin B. Lingaraju,^{1,*} Hsuan-Hao Lu,¹ Suparna Seshadri,¹
Daniel E. Leaird,¹ Andrew M. Weiner,¹ and Joseph M. Lukens²

¹*School of Electrical and Computer Engineering and Purdue Quantum Science and Engineering Institute, Purdue University, West Lafayette, Indiana 47907, USA*

²*Quantum Information Science Group, Computational Sciences and Engineering Division, Oak Ridge National Laboratory, Oak Ridge, Tennessee 37831, USA*

(Dated: October 21, 2020)

Flexible-grid wavelength-division multiplexing is a powerful tool in lightwave communications for maximizing spectral efficiency. In the emerging field of quantum networking, the need for effective resource provisioning is particularly acute, given the generally lower power levels, higher sensitivity to loss, and inapplicability of digital error correction. In this Letter, we leverage flex-grid technology to demonstrate reconfigurable distribution of quantum entanglement in a four-user tabletop network. By adaptively partitioning bandwidth with a single wavelength-selective switch, we successfully equalize two-party coincidence rates that initially differ by over two orders of magnitude. Our scalable approach introduces loss that is fixed with the number of users, offering a practical path for the establishment and management of quality-of-service guarantees in large quantum networks.

Quantum technology offers the promise of dramatic computational speed up [1] and security [2] beyond the capabilities of classical resources. Within this overall landscape, the development of quantum networks is critical for interconnecting quantum resources for applications such as blind quantum computing, quantum sensors, and distributed quantum computation [3]. While the specific design of such networks remains an active area of research, to the greatest extent possible any solution should integrate seamlessly into the existing fiber-optic infrastructure, while also leveraging advanced techniques in modern lightwave communications.

To this end, an efficient quantum networking approach gaining traction in recent years is based on entanglement distribution by a central provider [4–10]. In this paradigm, broadband polarization-entangled photons are carved into a series of spectral slices, which are then distributed to different users in the network. Since these photons are also entangled in the time-frequency degree of freedom, nonclassical polarization correlations are shared only between users who receive energy-matched channels. Recently, Wengerowsky *et al.* [9] demonstrated a fully and simultaneously connected QKD network by multiplexing multiple spectral slices to each user such that polarization entanglement exists between every possible two-party link. This elegant demonstration relies only on passive components, namely, a hierarchical tree of dense wavelength-division multiplexing (DWDM) filters. However, extending to significantly larger networks is a challenge, as the number of filters scales quadratically with the number of users N : a total of $2N^2 - 3N$ DWDMs are needed for full connectivity [9]. Follow-on work [11] made use of 50 : 50 beam splitters to reduce the number of DWDMs in this architecture by having two users share each spectral slice. However, this comes

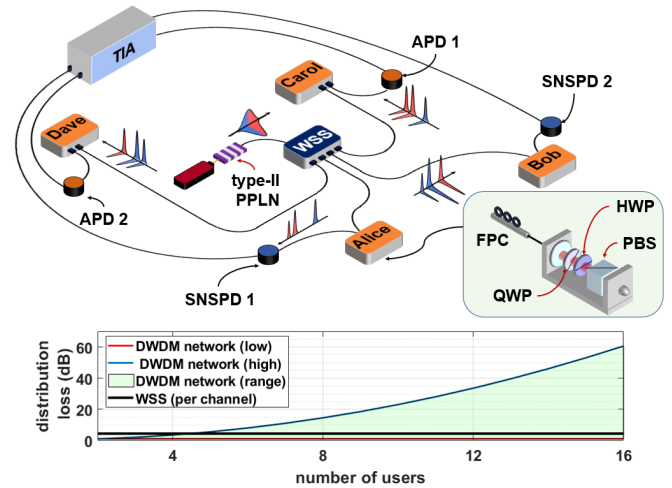


FIG. 1. Network testbed for adaptive entanglement distribution. The inset shows the spread and scaling of channel losses for an alternative DWDM approach compared to the WSS. See text for details.

at the expense of higher noise due to the intrinsic loss of 3 dB splitting.

In this Letter, we propose and demonstrate a significantly improved approach to entanglement distribution. In lieu of passive optical elements, we use a wavelength-selective switch (WSS) to apportion the biphoton bandwidth between users on a network. This approach provides a clear advantage in terms of network scalability as the loss incurred during entanglement distribution is independent of the number of users, imparting no additional decoherence on the polarization-encoded quantum states due to the WSS's polarization-diversity design. Furthermore, the bandwidth allocation can be reconfigured dynamically with simple electronic control. Consequently, the central provider can not only enable a fully and simultaneously connected network, but any arbitrary

* navin@purdue.edu

subgraph. Lastly, the bandwidth of spectral slices routed to each user can be modified, thus making it possible to boost or throttle the entanglement rate for a particular two-party link without modifying the pair source, pump laser, or physical links on the network. Until there is broader deployment of quantum networks in general, what criteria or communications priorities should guide the distribution of entanglement will remain unclear. Yet our work highlights how the use of flexible and reconfigurable bandwidth provisioning can optimize network performance with regard to a preferred criterion or outcome.

Our testbed is illustrated in Fig. 1. Time-energy entangled photons are generated by spontaneous parametric down-conversion in a periodically poled lithium niobate ridge waveguide (PPLN; HCP Photonics). The PPLN is engineered for type-II phase matching and is pumped by a ~ 24 mW continuous-wave laser ($\lambda \approx 780$ nm) [12]. In order to generate photon pairs also entangled in polarization, we match the pump wavelength and PPLN temperature to ensure spectrally degenerate down conversion [13]. Temporal walk-off between horizontally and vertically polarized components of the biphoton is compensated with a 90° splice of polarization-maintaining (PM) fiber with proper length. As a result, any two energy-matched spectral slices ($\omega_{\text{signal}} + \omega_{\text{idler}} = \omega_{\text{pump}}$) are polarization-entangled, ideally in the form $|\Psi\rangle \propto |HV\rangle + e^{i\phi} |VH\rangle$. For entanglement distribution, the output of the PPLN is sent to a WSS, which can multiplex arbitrary spectral slices across the C- and L-bands to any one of four output ports. The only limitation on this programmability is the resolution of the WSS (~ 20 GHz), which sets a lower bound on the bandwidth of individual slices. Subject to this bound, the WSS imparts equal losses for all connections up to the number of its output fibers.

On the other hand, the equivalent DWDM network presents widely varying loss across different channels as the number of users increases. While one channel need only travel through two DWDM filters, the worst-case spectral band must undergo, at the very least, $N^2 - N$ reflections followed by 1 transmission [9]. As an example, Fig. 1 (inset) compares loss for fully connected networks assuming 4.5 dB loss for the WSS version (matching our specific device) and 0.25 dB (0.6 dB) for reflection (transmission) from each DWDM filter. Below four users, the DWDM approach is more efficient, but this rapidly changes as the network size increases, with a worst-case channel loss reaching 60 dB at the 16-user mark. We suspect it may be possible to design more balanced DWDM configurations that mitigate this wide loss spread, yet the fundamental quadratic scaling should still remain.

The users, identified as Alice, Bob, Charlie, and Dave (see Fig. 1), are each equipped with a polarization analysis module that includes a fiber-based polarization controller (FPC), quarter-wave plate (QWP), half-wave plate (HWP), polarizer, and single-photon detector. The FPC compensates for rotation of the polarization state

that occurs during transmission between the source and the QWP. While the manual FPC can map the state of polarization from the HV basis of the source to the HV basis of the polarization analysis module, there remains an undetermined phase between the H and V states. We compensate for this unknown phase by orienting all QWPs at 45° , followed by additional rotation of HWP settings, for polarization correlation measurements in the diagonal-antidiagonal (DA) basis [14]. The HWP angle at which maximum contrast is obtained corresponds to the “effective” DA basis; concretely, we set the angle such that the ideal quantum state is $|\Psi^-\rangle \propto |HV\rangle - |VH\rangle$. (We note that, with additional detectors for simultaneous HV and DA monitoring [15] or automated feedback with classical reference pulses [16], it would be possible to compensate this directly with the FPC and remove the QWP.) Photons exiting the polarizer are routed to single-photon detectors for coincidence detection.

Of the four detectors used in this testbed, two are superconducting nanowire single-photon detectors (SNSPDs) while two are InGaAs avalanche photodiodes (APDs). The free-running SNSPDs used by Alice and Bob have quantum efficiencies ~ 0.85 . The InGaAs APDs, which are allocated to Charlie and Dave, are gated with a 20 MHz clock (10% duty cycle) and have quantum efficiencies of ~ 0.2 and ~ 0.1 , respectively. When the WSS is programmed to operate as a multiport (1 : 4) beam splitter for the whole biphoton bandwidth, the average singles count rates at each user are 2.6×10^5 s $^{-1}$ (Alice), 3.3×10^5 s $^{-1}$ (Bob), 5.5×10^3 s $^{-1}$ (Charlie), and 3.3×10^3 s $^{-1}$ (Dave), highlighting the vast disparity between the two classes of detectors.

Prior to apportioning the biphoton bandwidth for entanglement distribution over the network, we characterize the entanglement after the WSS using Alice’s and Bob’s polarization analysis modules. The biphoton spectrum is carved into 24 spectral slices, each of which is 24 GHz wide, and includes a central stopband [see Fig. 2(a)]. This channel width is chosen to match an integer multiple of the effective 4 GHz addressability of the WSS (owing to how pixels in the device’s spatial light modulator are wired together) while still exceeding its ~ 20 GHz spectral resolution. We define a channel as a pair of such energy-matched spectral slices. Fidelity with respect to the $|\Psi^-\rangle$ Bell state is determined by measurements in two sets of mutually unbiased bases [coincidences in HV and DA bases are shown in Fig. 2(b)]. Despite the tomographic incompleteness of this two-basis-pair set, our use of Bayesian mean estimation [17, 18] nevertheless enables us to obtain meaningful state estimates, which due to the high correlations obtained also contain low uncertainty. Our measurement results using the Bayesian tomography workflow of Ref. [19] are presented in Fig. 2(c). For channels 1–11, which span most of the biphoton bandwidth, we are able to measure fidelities higher than 95%, which illustrates both the quality of polarization rotation compensation and the stability of the WSS’s polarization diversity scheme.

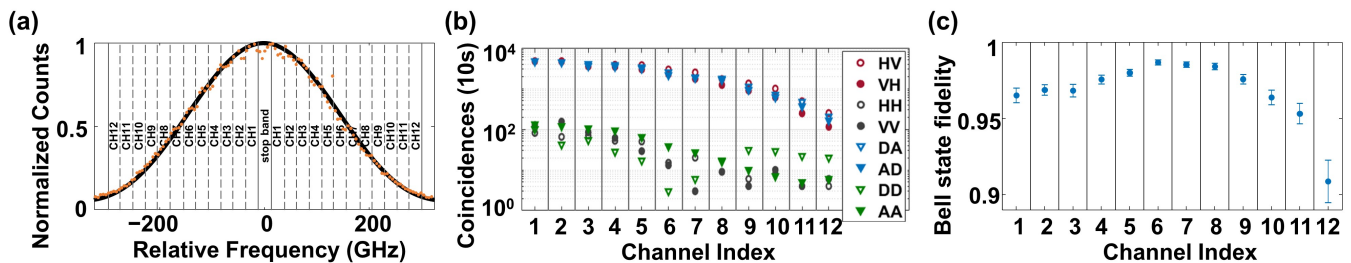


FIG. 2. (a) Sinc-squared fit to the normalized singles rate as a function of detuning from the center of the biphoton spectrum. The locations of 12 pairs of energy-matched spectral slices are overlaid on the spectrum. (b) Data from polarization-correlation measurements in the rectilinear (HV) and diagonal (DA) bases, measured between Alice and Bob for all 12 channels. (c) Corresponding Bell state fidelities computed using Bayesian quantum state tomography.

The four-user network illustrated in Fig. 1 comprises six possible two-party connections, called links, each of which is assigned a unique color in Fig. 3. The down-converted photons pass to the WSS for wavelength-multiplexed distribution to Alice, Bob, Charlie, and Dave, and we add suitable electronic offsets to the outputs of each detector to position the coincidence peaks for all six links in multiples of 10 ns apart. We use a coincidence window of 1024 ps, which exceeds the jitter of all detector pairs.

We first consider the case of wavelength-multiplexed entanglement distribution based on a fixed 48 GHz grid, corresponding to a total of 6 equal-width pairs from the 12 channels defined in Fig. 2(a). The biphoton bandwidth, counting from the center out, is allocated to the different links based on alphabetical ordering, i.e., Alice–Bob (AB), Alice–Charlie (AC), Alice–Dave (AD), Bob–Charlie (BC), Bob–Dave (BD), and Charlie–Dave (CD). Figure 3(a) shows two-photon events recorded between all six links. Note the extremely low counts of link CD, due to the fact it combines the two least efficient channels and, under this distribution scenario, also receives the pair of 48 GHz spectral slices with the lowest flux. While far from optimal in terms of balancing two-party coincidence rates, this configuration might alternatively be interpreted as boosting service for a premium link, Alice–Bob in this case. Thus even in this example, we see the value of flexible bandwidth allocation in configuring the network for different needs, such as diverse quality-of-service targets. Nevertheless, to better balance coincidence rates across all six links, we next reallocate the biphoton bandwidth on the same fixed 48 GHz spectral grid. Now, brighter slices are routed to the less-efficient links. Figure 3(b) shows histograms of two-photon events for all user-to-user connections. While the previous scenario saw a ratio of ~ 4200 in the coincidence rates of links AB and CD, that imbalance is now only ~ 26 .

Moving from fixed-grid distribution to a more flexible provisioning of bandwidth, we lastly utilize the 12 channels defined in Fig. 2(a), but do not place any limitations on how they are allocated between the different links. Aiming to equalize coincidence rates across the network, we provision the spectrum as shown in Fig. 3(c); we no

longer enable a fully connected network because link CD would not even in the most favorable allocation (sending 7 channels with the highest pair flux) be able to reach coincidence rates comparable to the other users. Therefore, we program the WSS to harmonize the coincidence rate among a subgraph of five links (all links except for CD). From Fig. 3(c) we see that all coincidence rates are within a factor of 2, a significant improvement over the fixed-grid cases.

Importantly, for the allocations of Fig. 3(b-c), balancing coincidence rates relies not only on link bandwidth, but also use of the full biphoton spectrum [Fig. 2(a)] – a departure from previous works which limited consideration to uniform-flux slices near the center of the spectrum [9, 11]. In our full-flex scenario in particular, interleaving channel allocations (e.g., for Links AC/BC and AD/BD) thereby allows us to equalize the mean flux for links of comparable detection efficiencies. While of course high flux across a broader bandwidth would always be preferred, our results show the value of flex-grid allocation under the constraints of limited entanglement resources in a network.

Moving forward, our approach should be readily extendable to many more users with only small modifications to the basic setup. While type-II phase-matching allows us to generate polarization-entangled photon pairs in a single-pass, single-crystal configuration, alternative sources based on type-0 or type-I nonlinear crystals (copolarized signal and idler) using Sagnac [4, 20] or Mach–Zehnder [6, 21] arrangements would enable the generation of polarization-entangled photon pairs with essentially uniform flux across the entire C-band. Coupled with current commercial WSSs with 20 output ports, 4.8 THz bandwidth, and 6.25 GHz resolution [22], a partitioning of 12.5 GHz slices would provide all $N(N-1)$ spectral channels necessary for a fully connected network of $N = 20$ users. This stands in stark contrast to the nested DWDM approach [9], for which increasing to 20 users would require a massive 740 DWDMs. Moreover, while a 20-user WSS could support full *simultaneous* connectivity, its ability to reconfigure bandwidth means this is not required; the service provider can adjust bandwidth channels on demand to

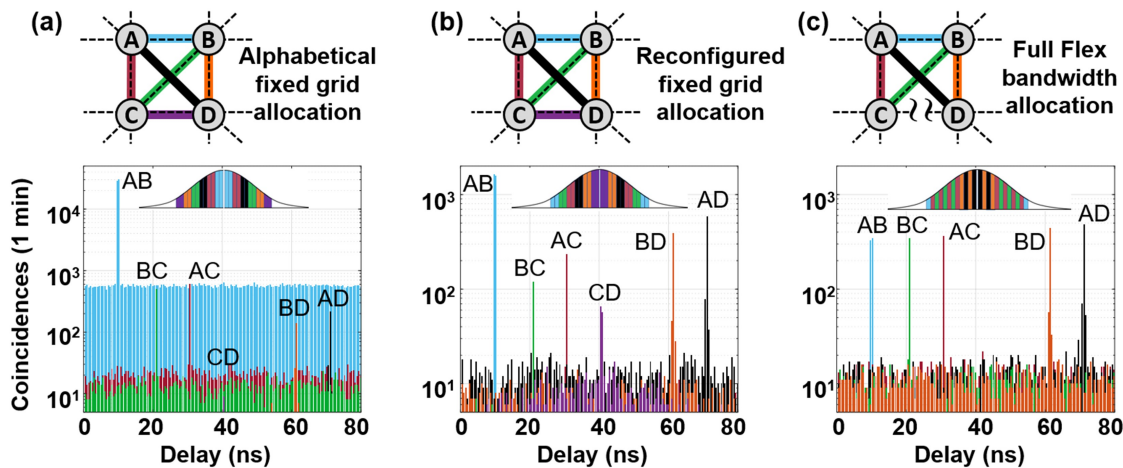


FIG. 3. (a) Coincidences for each two-party link based on a fixed 48 GHz grid, allocated alphabetically. The inset illustrates how the biphoton bandwidth is shared between all six links. (b) Coincidences for a fixed 48 GHz grid with channels allocated to best balance rates among all links. (c) Full-flex configuration with 24 GHz-wide spectral slices allocated freely between users to harmonize coincidence rates across a subgraph of the network. Link CD (APD-APD) is unable to be equalized and is dropped.

realize *any* network subgraph, allocating unused bandwidth to increase entanglement rates in other channels. Such adaptivity makes the WSS approach superior in terms of latent resources compared to passive configurations.

In the present experiment, our quality-of-service metric focused on the coincidence rate between each pair of users. Although indicative of network performance, it does not directly reflect state fidelity – crucial to quantum information protocols. In future work, through a combination of state tomography or entanglement witnesses, it should be possible to quantify the entanglement quality of each link in terms of ebits/s, which incorporates both detection rate and fidelity into a single metric, and then apportion bandwidth to equalize this target appropriately. Finally, while here we utilize frequency entanglement to establish bipartite correlations – with polarization as the information carrier – it is also possible to leverage the frequency degree of freedom directly for quantum information processing [23, 24]. While typically considered in a single-polarization context, recent demonstrations of polarization-diversity phase modulation [25, 26] indicate the potential to exploit both

frequency and polarization in parallel for carrying and processing quantum information for even more flexible quantum networks.

Funding. U.S. Department of Energy, Office of Science, Office of Advanced Scientific Computing Research (Early Career Research Program); National Science Foundation (NSF) (1839191-ECCS, 1747426-DMR); Oak Ridge National Laboratory (Laboratory Directed Research and Development).

Acknowledgments. Some preliminary results for this article were presented at CLEO 2020 as paper number FTh5D.2. We thank P. Imany, M. Alshowkan, B. Qi, and N. A. Peters for discussions. We also thank N. Knight and O. E. Sandoval for helping with temporal walk-off compensation. A portion of this work was performed at Oak Ridge National Laboratory, operated by UT-Battelle for the U.S. Department of Energy under contract no. DE-AC05-00OR22725

Disclosures. The authors declare no conflicts of interest.

[1] T. D. Ladd, F. Jelezko, R. Laflamme, Y. Nakamura, C. Monroe, and J. L. O’Brien, *Nature* **464**, 45 (2010).
 [2] N. Gisin and R. Thew, *Nat. Photon.* **1**, 165 (2007).
 [3] S. Wehner, D. Elkouss, and R. Hanson, *Science* **362**, eaam9288 (2018).
 [4] H. C. Lim, A. Yoshizawa, H. Tsuchida, and K. Kikuchi, *Opt. Express* **16**, 22099 (2008).
 [5] M. Brodsky and M. D. Feuer, U.S. Patent Publication 2009/0180616 A1 (2009).

[6] I. Herbauts, B. Blauensteiner, A. Poppe, T. Jennewein, and H. Hübel, *Opt. Express* **21**, 29013 (2013).
 [7] A. Ciurana, V. Martin, J. Martinez-Mateo, B. Schrenk, M. Peev, and A. Poppe, *IEEE J. Sel. Top. Quantum Electron.* **21**, 6400212 (2015).
 [8] D. Aktas, B. Fedrici, F. Kaiser, T. Lunghi, L. Labonté, and S. Tanzilli, *Laser Photonics Rev.* **10**, 451 (2016).
 [9] S. Wengerowsky, S. K. Joshi, F. Steinlechner, H. Hübel, and R. Ursin, *Nature* **564**, 225 (2018).

- [10] E. Y. Zhu, C. Corbari, A. Gladyshev, P. G. Kazansky, H.-K. Lo, and L. Qian, *J. Opt. Soc. Am. B* **36**, B1 (2019).
- [11] S. K. Joshi, D. Aktas, S. Wengerowsky, M. Lončarić, S. P. Neumann, B. Liu, T. Scheidl, G. C. Lorenzo, Ž. Samec, L. Kling, A. Qiu, M. Razavi, M. Stipčević, J. G. Rarity, and R. Ursin, *Sci. Adv.* **6**, eaba0959 (2020).
- [12] G. Fujii, N. Namekata, M. Motoya, S. Kurimura, and S. Inoue, *Opt. Express* **15**, 12769 (2007).
- [13] E. Y. Zhu, Z. Tang, L. Qian, L. G. Helt, M. Liscidini, J. E. Sipe, C. Corbari, A. Canagasabey, M. Ibsen, and P. G. Kazansky, *Opt. Lett.* **38**, 4397 (2013).
- [14] N. Peters, J. Altepeter, E. Jeffrey, D. Branning, and P. Kwiat, *Quantum Inf. Comput.* **3**, 503 (2003).
- [15] A. Poppe, A. Fedrizzi, R. Ursin, H. R. Böhm, T. Lorünser, O. Maurhardt, M. Peev, M. Suda, C. Kurtsiefer, H. Weinfurter, T. Jennewein, and A. Zeilinger, *Opt. Express* **12**, 3865 (2004).
- [16] A. Treiber, A. Poppe, M. Hentschel, D. Ferrini, T. Lorünser, E. Querasser, T. Matyus, H. Hübel, and A. Zeilinger, *New J. Phys.* **11**, 045013 (2009).
- [17] R. Blume-Kohout, *New J. Phys.* **12**, 043034 (2010).
- [18] B. P. Williams and P. Lougovski, *New J. Phys.* **19**, 043003 (2017).
- [19] J. M. Lukens, K. J. H. Law, A. Jasra, and P. Lougovski, *New J. Phys.* **22**, 063038 (2020).
- [20] P. Vergyris, F. Kaiser, E. Gouzien, G. Sauder, T. Lunghi, and S. Tanzilli, *Quantum Sci. Technol.* **2**, 024007 (2017).
- [21] A. Yoshizawa and H. Tsuchida, *Appl. Phys. Lett.* **85**, 2457 (2004).
- [22] Finisar, “Single wavelength selective switch (WSS),” https://finisarwss.com/wp-content/uploads/2020/07/FinisarWSS_Single_Wavelength_Selective_Switch_ProductBrief_Jun2020.pdf (2020).
- [23] J. M. Lukens and P. Lougovski, *Optica* **4**, 8 (2017).
- [24] H.-H. Lu, A. M. Weiner, P. Lougovski, and J. M. Lukens, *IEEE Photon. Technol. Lett.* **31**, 1858 (2019).
- [25] O. E. Sandoval, N. B. Lingaraju, P. Imany, D. E. Leaird, M. Brodsky, and A. M. Weiner, *Opt. Lett.* **44**, 1674 (2019).
- [26] N. B. Lingaraju, N. O’Malley, D. E. Jones, O. E. Sandoval, H. N. Azzouz, D. E. Leaird, J. M. Lukens, M. Brodsky, and A. M. Weiner, in *CLEO: QELS* (Optical Society of America, 2020) p. FF1D.5.